Design of optimized wave-optical spheroidal nanostructures for photonic-enhanced solar cells

Manuel J. Mendes *, Andreia Araújo, António Vicente, Hugo Águas, Isabel Ferreira, Elvira Fortunato, Rodrigo Martins

i3N/CENIMAT, Department of Materials Science, Faculty of Science and Technology, Universidade NOVA de Lisboa and CEMOP/UNINOVA, Campus de Caparica, 2829-516 Caparica, Portugal

A B S T R A C T

The interaction of light with wavelength-sized photonic nanostructures is highly promising for light management applied to thin-film photovoltaics. Several light trapping effects come into play in the wave optics regime of such structures that crucially depend on the parameters of the photonic and absorbing elements. Thus, multi-parameter optimizations employing exact numerical models, as performed in this work, are essential to determine the maximum photocurrent enhancement that can be produced in solar cells.

Generalized spheroidal geometries and high-index dielectric materials are considered here to model the design of the optical elements providing broadband absorption enhancement in planar silicon solar cells. The physical mechanisms responsible for such enhancement are schematized in a spectral diagram, providing a deeper understanding of the advantageous characteristics of the optimized geometries. The best structures, composed of TiO_2 half-spheroids patterned on the cells' top surface, yield two times higher photocurrent (up to 32.5 mA/cm^2 in 1.5 μm thick silicon layer) than the same devices without photonic schemes.

These results set the state-of-the-art closer to the theoretical *Lambertian* limit. In addition, the considered light trapping designs are not affected by the traditional compromise between absorption enhancement versus current degradation by recombination, which is a key technological advantage.

© 2016 Elsevier Ltd. All rights reserved.

1. Introduction

The large mismatch between the light absorption depth and the carrier diffusion length, in deposited thin semiconductor films, makes light management crucial for the realization of high-efficient (> 25%) and inexpensive (< 0.5$/W) non-wafer-based solar cells [1]. Optimized light trapping (LT) strategies have the potential to strongly boost the optical absorption in the thin solar cell material, thereby enhancing the efficiency and allowing the thickness reduction. Optically-thicker but physically-thinner devices imply cheaper and faster fabrication, and also improved flexibility which is important for roll-to-roll manufacturing [2] and their application in bendable substrates (e.g. paper [3], polymers, tissues, etc.) aimed for consumer-oriented products (sun-powered intelligent packaging [4], wearable PV, portable electronics, etc). In addition, for cells not limited by surface recombination, a reduction in their thickness can lead to higher open-circuit voltages (and consequently efficiencies) due to lower bulk recombination [5].

The conventional LT approach is the insertion of textured surfaces at the rear or front of the solar cells, to diffuse light and thus increase its optical path length within the absorber layer [6–9]. In the last decade, a variety of more advanced strategies have been proposed employing: self-assembled plasmonic metal nanoparticles [10,11], diffraction gratings [12–14], photonic crystals [15], optical resonators [16,17], among others. These make use of the scattering and/or anti-reflection properties of nanophotonic elements, with dimensions comparable or below the illuminating wavelengths, incorporated in the cells. Nevertheless, both wafer-based and thin film PV industries still prefer employing the standard LT mechanism based in surface texturing. The reason is that, even though many LT methods are able to provide high optical gains, they also present practical drawbacks, which hinder their implementation. For instance, the resonant scattering effects of plasmonic nanoparticles have attracted much attention to enhance the optical path length of the near-infrared (NIR) light close to the silicon bandgap [18,19]. However, such scatterers also exhibit significant parasitic absorption, which hampers the efficiency gains that they can provide. Alternatively, 2D grating wavelength-sized corrugations, formed by nanostructuring the absorber layer

or the substrate, have been shown to provide effective light scattering combined with gradual refractive index matching for anti-reflection when implemented on the cells' front surface (e.g. arrays of domes [20], cylinders [21], dimples [22], quasi-random patterns [23]), but without the associated parasitic absorption. However, such approaches are affected by the same key issue of texturing: an effective LT requires structuring the surface of the cell material, thereby increasing the amount of defects and surface area of the device which increases the charge carriers capture and recombination [24,25]. Consequently, the improvement of the cells' optical performance comes at the expense of a reduction in their electrical performance, which is a severely limiting trade-off.

This calls for further constraints that should be applied to the theoretical design of the LT structures, focusing in solutions that can be truly effective in practice. The present study is aimed at circumventing the aforementioned drawbacks of LT approaches, by following three key design principles:

1) Planar absorber layer – the LT structures should not increase the surface area of the photocurrent-generating layer, in order to prevent the increase of recombination in the cell. As such, the structures considered here are optimized for light absorption enhancement in perfectly-flat PV layers, thereby not affecting the cells' electrical performance.
2) Lossless optical materials – since the LT structures are incorporated on the front cell surface, their material should have negligible absorption in the spectral range of the cell photocurrent. Here we consider photonic elements made solely of dielectric materials, i.e. TiO$_2$ and transparent conductive oxides (TCOs), with a low imaginary part of the refractive index in the wavelengths of interest.
3) Round geometries – the optical elements considered here are based in spheroidal or semi-spheroidal geometries [26], as most scattering features can be approximated by such shapes. Round shapes are preferable to those with corners or edges (e.g. typical texturing features, nano-cones, cylinders/wires, etc. [9]) because sharp terminations produce strongly-localized near-fields whose energy is generally dissipated as heat and not used for current generation. Furthermore, spheroidal geometries can exhibit lower sensitivity to the angle of incidence of the illumination, in comparison with anti-reflection coatings [5,17,27,28], which is important to increase the acceptance angle of non-tracking PV devices.

High-index dielectric features having dimensions comparable to the illuminating wavelengths can exhibit significant anti-reflection and forward-scattering capabilities, which make them highly promising for application in the front surface of thin film cells [1,28,29] as those considered here composed of amorphous (a-Si:H) or crystalline silicon (c-Si) absorber materials. Carefully-engineered front structures, composed of non-absorbing elements (e.g. dielectric particles), provide an effective pathway for the light to flow into the absorber layer and get trapped there. Such structures can be compatible with the three previously listed design principles when implemented on top of already completed solar cells, which is an important practical advantage. Due to their wavelength-scale dimensions, such elements interact with light in an intermediate size regime between geometrical optics and electrostatics, known as the wave optics regime, whose solutions require the detailed calculation of the set of Maxwell's equations, and no analytical approximations can be used such as in the other regimes. Therefore, a numerical mesh-based FDTD formalism is employed to model the electric-field distribution produced in the structures considered here.

Recently, current enhancement in solar cells has been demonstrated by coating their front TCO layer with a monolayer of dielectric wavelength-sized particles such as arrays of close-packed silica spheres [16,17], TiO$_2$ pyramids [27], among others [1,28]. The properties of such wave-optical structures crucially depend on their geometry and material. For instance, particle shapes with higher aspect ratio exhibit a stronger anti-reflection action which leads to absorption enhancement mainly in the short wavelength range (UV–vis); while lower aspect ratio enables a more effective light scattering and coupling to waveguided modes of the cell, which contributes to absorption mainly for the longer NIR wavelengths. Therefore, it is essential to perform complete optimizations of the full set of relevant parameters (refractive index, dimensions, particle-cell and inter-particle spacing, etc.), as performed here, in order to realize truly pronounced broadband LT and attain exceptional improvements in the cells performance.

In this work, the exploration of a broad set of physical parameters of the LT features allowed us to demonstrate remarkable broadband gains in the cells absorption, relative to those reported in the related literature of photonic-enhanced thin film PV where complete optimization studies are scarcely performed. This enabled the determination of LT structures capable of producing short-circuit current density (J$_{SC}$) values (up to 32.5 mA/cm^2 in

Table 1.
Maximum J$_{SC}$ values attained for the optimized light trapping (LT) structures placed on the two types of solar cells, with distinct Si absorber layers, considered in this work. The optimal parameters of the structures are defined in Figs. 1 and 5: ARC thickness (t), particle refractive index (N_R), particle semi-axis along (R) and orthogonal (R_Z) to the plane of the cell layers, inter-particle distance (D).

Light Trapping Structure	Materials	PV absorber layer: **300 nm a-Si**		PV absorber layer: **1.5 μm c-Si**		Row Label
		Optimal Parameters	J$_{SC}$ (mA/cm^2)	Optimal Parameters	J$_{SC}$ (mA/cm^2)	
ARC layer (Fig. 2)	No layer	–	**17.5**	–	**16.4**	A1
	AZO	t=71 nm	**25.4**	t=68 nm	**21.7**	A2
Spheroid partially embedded in ARC layer (Fig. 3)	Lossless dielectric (index N_R) in AZO	N_R=2.48 R=309.7 nm R_Z=346.6 nm t=280.1 nm	**30.4**	N_R=2.99 R=404 nm R_Z=290.1 nm t=209.7 nm	**30.5**	B1
	TiO$_2$ in AZO	R=322.2 nm R_Z=363.2 nm t=303 nm	**30.2**	R=403.6 nm R_Z=274.9 nm t=127.1 nm	**29.8**	B2
Half-spheroid (Fig. 4)	TiO$_2$	R=565.0 nm R_Z=990.0 nm	**31.9**	R=463.1 nm R_Z=796.2 nm	**32.5**	C
Hexagonal array of half-spheroids (Fig. 5)	TiO$_2$ in AZO	R=344.1 nm R_Z=1373 nm D=985.9 nm t=64.5 nm	**31.4**	R=368.0 nm R_Z=826.5 nm D=997.2 nm t=65.7 nm	**31.1**	D
Lambertian limit (Fig. S1)	–	–	**33.7**	–	**38.0**	E

1.5 μm thick c-Si) which are ~50% higher than those attained (21.7 mA/cm²) with an optimized anti-reflection coating and ~100% higher than a cell with no LT (16.4 mA/cm²), as shown in Table 1 below. Such optimal structure yields a current similar to that (32.9 mA/cm²) of a state-of-the-art thin film (~4 μm) Si single-junction [22], fabricated on a periodically honeycomb-textured substrate, but using a much thinner Si layer. The absorption and J_SC generated in the cells with the optimized LT structures are also compared here with the ideal geometrical optics reference case of a *Lambertian* scattering surface [8,14].

2. Numerical methods

A 3D finite-difference time domain (FDTD) numerical method [30] is employed to rigorously model the optical effects of wavelength-sized dielectric particles on thin film solar cells. The method solves Maxwell's equations in arbitrary geometries and materials, being one of the preferential approaches to tackle electromagnetic problems in the wave-optics regime, particularly for PV light management, due to its conceptual simplicity, versatility, and since it is a time-domain method the solutions can cover a wide frequency range with a single simulation run [1,17,21,25,31].

Dielectric objects with sizes close to or above the illuminating wavelength scatter the light preferentially along the incident wave propagation direction (forward scattering). For instance, resonant spheroidal particles have been shown to produce remarkably intense electric near fields close to their shadow-side surface [29] and act as effective nanostructured anti-reflection coatings (ARCs) on the front surface of thin film Si cells [17]. Therefore, one of the first base structures analyzed in this work is that represented in Fig. 1, showing the main parameters taken as variables for the optimization studies. The represented square unit cell (see Fig. 1b) simulates one period of a square array of close-packed particles placed on the front TCO contact of a Si solar cell with arbitrarily large area. The FDTD program places the unit cell in a square box with specific boundary conditions (BCs) in each face. An artificial absorbing perfect-matching layer is applied on the upper boundary (z_MAX) to absorb all outgoing waves. A perfect metal BC is used on the front surface of the rear mirror (z_MIN) to simulate a perfect reflecting layer. On the side boundaries (x,y), periodic BCs are used to model the infinite periodicity of the structures and the normally incident plane wave source. Here, symmetric and anti-symmetric

BCs are employed to reduce the required memory size and computation time. This is possible due to the symmetry of the geometry and the orientation of the illuminating field (incident along the z axis), which allows to simulate only one quadrant (red region of Fig. 1b) of the unit cell.

To simulate solar illumination, a broadband plane wave source is placed in the air medium above the structure. The source bandwidth is 400–1100 nm, since the AM1.5 solar photon flux outside this wavelength range is small, and it corresponds to the most significant portion of the photocurrent spectrum of Si-based PV devices.

The optical properties of the materials composing the structures are determined by their standard complex refractive index functions, retrieved from usual references [30,32,33]. The power absorbed per unit volume (P_ABS) in each element of the structures is given by the resulting electric field distribution established in their material:

$$P_{ABS} = \frac{1}{2}\omega\epsilon''|\mathbf{E}|^2 \tag{1}$$

where $|\mathbf{E}|^2$ is the electric field intensity, ω is the angular frequency of the light and ϵ'' is the imaginary part of the dielectric permittivity. P_ABS is normalized by the source power to obtain the absorption per unit volume, p_ABS (units of m^{-3}). The total light absorption in a region, at a certain wavelength (λ), is computed by integrating p_ABS over its volume: $Abs(\lambda) = \int p_{ABS}(\lambda)dV$. The only absorption that generates current is that occurring in the Si layer, while that occurring in the other layers is parasitic as it corresponds to optical losses. Since we are mainly concerned with the optical rather than the electrical transport properties of the cells, an internal quantum efficiency equal to one is assumed (i.e. every photon absorbed in Si generates carriers collected by the contacts). As such, the short-circuit current density (J_SC) is determined by integrating the absorption in the Si layer, convoluted with the incident AM1.5 solar power spectrum (I_AM1.5, units of W m⁻² m⁻¹), over the computed wavelength range (400–1100 nm):

$$J_{SC} = e \int \frac{\lambda}{hc} Abs(\lambda) I_{AM1.5}(\lambda) d\lambda \tag{2}$$

where e is the electronic charge, h is the Planck constant and c is the free space light speed. This spectrally-integrated J_SC can be regarded as an upper limit corresponding to the ideal case of no electrical losses, and is taken here as the figure of merit to optimize the performance of the photonic structures.
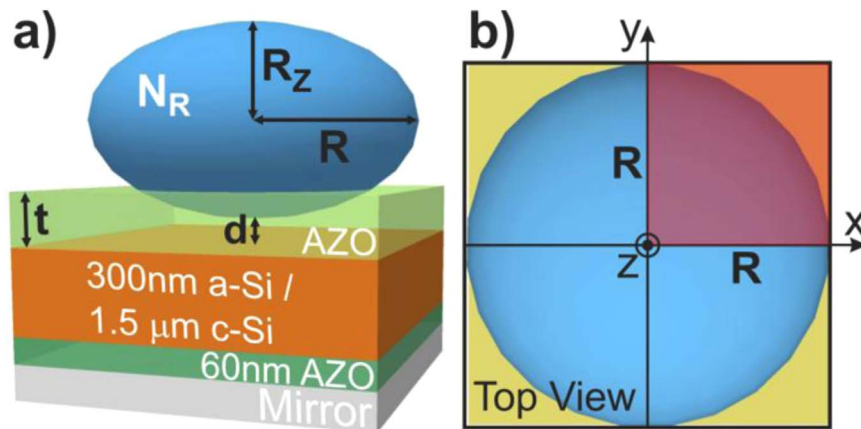
Fig. 1. Sketch of the unit cell of a square array simulated in this work, representing the parameters (N_R, R, R_Z, t, d) considered for optimization. a) Spheroids with a real refractive index N_R are the photonic elements used to trap light in a thin silicon (either a-Si or c-S) film located at a distance d from the bottom of the spheroid. The light impinges from the top along its axis of revolution (z). The dimensions of the spheroid are given by its semi-axes along (R_Z) and orthogonal (R) to the illumination axis. The front and rear contacts of the cell structure are, respectively, an AZO layer with thickness t and a back-reflector composed by a 60 nm AZO layer and a perfect mirror. b) Top view of the simulated structure, with the coordinate axes, whose symmetry allows the computed region to be reduced to the volume in red.

A *particle swarm* optimization algorithm was used in the FDTD programs to search for the optimal parameters of the LT elements (sketched in Fig. 1) that yield the highest J_{SC}. This is a population-based stochastic optimization technique widely used for various PV and photonic design problems [34]. The algorithm iteratively adjusts the geometry and material of the LT structures to maximize the light absorption in the Si region, while minimizing the optical losses (i.e. total reflection and absorption occurring in the TCO layers and dielectric spheroids).

3. Optimized photonic structures

Recent trends in PV indicate that, in the coming decade, the solar electricity market should have a major component of inexpensive and flexible thin film devices, fabricated using large-scale roll-to-roll processes [2,3,28]. However, it is only possible for thin film solar cells to reach the stage of efficiencies (20–25%) of typical crystalline wafer-based Si cells by implementing advanced light management procedures compatible with the industrial scalability requirements. Previous contributions have shown that dielectric features with nano/micron-scale sizes on the order of λ are the preferential photonic structures for PV LT [1,28,29]. Among the various techniques that allow engineering such structures, it is desirable to focus in those that are truly low-cost and scalable, as these are key requirements in PV. As such, ordered arrays of colloidal dielectric particles are interesting to consider, as they can be formed by fast and inexpensive wet-coating methods, straight-forwardly adaptable to roll-to-roll manufacturing, while allowing a precise control and monodispersion in the particles' sizes [16,17]. Reactive ion-etching post-treatments performed on the deposited spherical colloids can shape their geometry and form mono-dispersed spheroidal particles with good control on the aspect ratio [20,28]. Tailoring the aspect ratio, together with the particles' material and size, enables a wide range of possibilities for tuning the particles' optical behavior [26,29] in order to strengthen the electric field intensity in nearby absorbing layers.

In view of the above, we start by considering spheroidal dielectric particles as the LT elements (see Fig. 1) and analyze the absorption enhancement occurring in the underneath cell layers, comparing it with that attained with an optimized single-layer anti-reflection coating. We analyze separately the results of the structures patterned on thin film cells with either a 300 nm thick a-Si:H or a 1.5 μm thick c-Si absorber layer (Fig. 1a). The former type of Si layer is the one more commonly employed in single-junction thin film devices; while the latter is motivated by the recently-demonstrated production of ultra-thin (1–20 μm) mono-crystalline Si wafers, regarded as the preferential material for the development of high-efficient thin cells coupled with LT approaches [24,25]. Such thin c-Si absorbers can potentially combine the advantages of wafer-based (e.g. high open-circuit voltage and fill factor) and thin film (e.g. low cost, flexibility) technologies. In addition, the thicknesses of both types of absorber layers are expected to enable considerable absorption enhancement upon the application of LT, as predicted analytically with a geometrical optics approximation analyzed in Section S1 of the Supplementary Material.

For both absorber layers, the parameters of the LT structures (sketched in Fig. 1a) were taken as variables to maximize the J_{SC} (Eq. (2)), using the optimization algorithm mentioned in Section 2. Appropriate domains were imposed on each variable, to restrict the search to reasonable regions in the parameter space: R and $R_Z < 2$ μm, $t < 0.5$ μm, $1 < N_R < 4$, $2R < D < 4R$. The algorithm performs a sequence of optimization steps, with distinct sets of initial values taken within the domains, until the global J_{SC} maximum is found. The final results are listed in Table 1 and are discussed along this section. Such results are compared with the well-known *Lambertian* light scattering limit of ray optics (in row E) [1,14,24], further detailed in Section S1 of the Supplementary Material, which is a common comparative limit for PV LT but not the fundamental limit in the wave optics regime [12,35].

3.1. Single-layer anti-reflection coating

The top layer of thin film Si cells is usually a transparent conductive oxide (TCO) with a double role in the device: electrically, it constitutes the front contact; while optically it reduces the reflection due to its adequate refractive index. Therefore, an optimized top TCO layer acts as an effective anti-reflection coating (ARC) and will be taken here as the reference LT mechanism to compare the absorption enhancements with those attained by the incorporation of the particle structures. Such layer will be henceforth designated as ARC, for simplicity. Usually it is made of ITO, since this material can exhibit a good tradeoff between a high broadband transparency and low electrical resistance. However, due to the scarcity of indium, ZnO-based oxides (mainly AZO) are regarded as more favorable alternatives for PV.

Section S2 of the Supplementary Material presents the results of the front ARC optimization studies, for the two types of cell structures considered in this work. The best J_{SC} values are obtained for AZO ARCs with the thicknesses (t) indicated in row A2 of Table 1. Since AZO has lower parasitic light absorption than ITO, the J_{SC} values are higher than those with ITO because the simulations are purely optical and do not take into account the conductivity of the materials. As such, AZO will be henceforth the material of the front ARC of our structures, as depicted in Fig. 1a.

Fig. 2a and c shows, respectively, the light absorption occurring inside and outside the 300 nm a-Si and 1.5 μm c-Si layers of the cells, with the optimized AZO ARCs on top ($t=71$ and 68 nm, respectively). The peak anti-reflection produced with an ARC occurs approximately when its thickness is a quarter of the wavelength in its dielectric material ($t=\lambda_{MAX}/4N_{AZO}$). This is consistent with the absorption maxima of Fig. 2a and c, occurring respectively at $\lambda=559$ nm and $\lambda=511$ nm, given the refractive index of AZO ($N_{AZO} \sim 1.8$ to 2). These absorption spectra are compared with those of structures without any ARC ($t=0$), which suffer from high reflection from the top Si surface for $\lambda < 750$ nm and therefore generate much lower currents (see row A1 of Table 1).

The optical losses occurring in the front and rear AZO layers (dashed curves in the plots) are practically negligible in the investigated spectral range. This can also be visualized in Fig. 2b and d which show the p_{ABS} profiles at the two wavelengths marked by the grey arrows in Fig. 2a and c, respectively. For shorter wavelengths (see profiles on the left), most absorption occurs up to a depth of 100 nm in the Si layer, while for longer wavelengths (right profiles) the absorption is distributed more uniformly along the layer depth.

In the considered spectral range, the absorption coefficient of a-Si is much higher than c-Si for wavelengths below ~ 700 nm, which explains the higher J_{SC} values achieved in the 300 nm a-Si cells (see Table 1). In real devices, the resulting J_{SC} would be different due to electrical effects, such as the layers resistivity and carrier recombination [5,7,21,25], not taken into account in this study since it is focused on the optimization of the optical response of the LT front structures.

3.2. Spheroids partially embedded in ARC

As seen in the previous sub-section, ARCs can suppress reflection but only in a narrow range around λ_{MAX}, for which the back-reflected light wave is minimized due to destructive interference. An array of dielectric nanostructures incorporated in the ARC is an
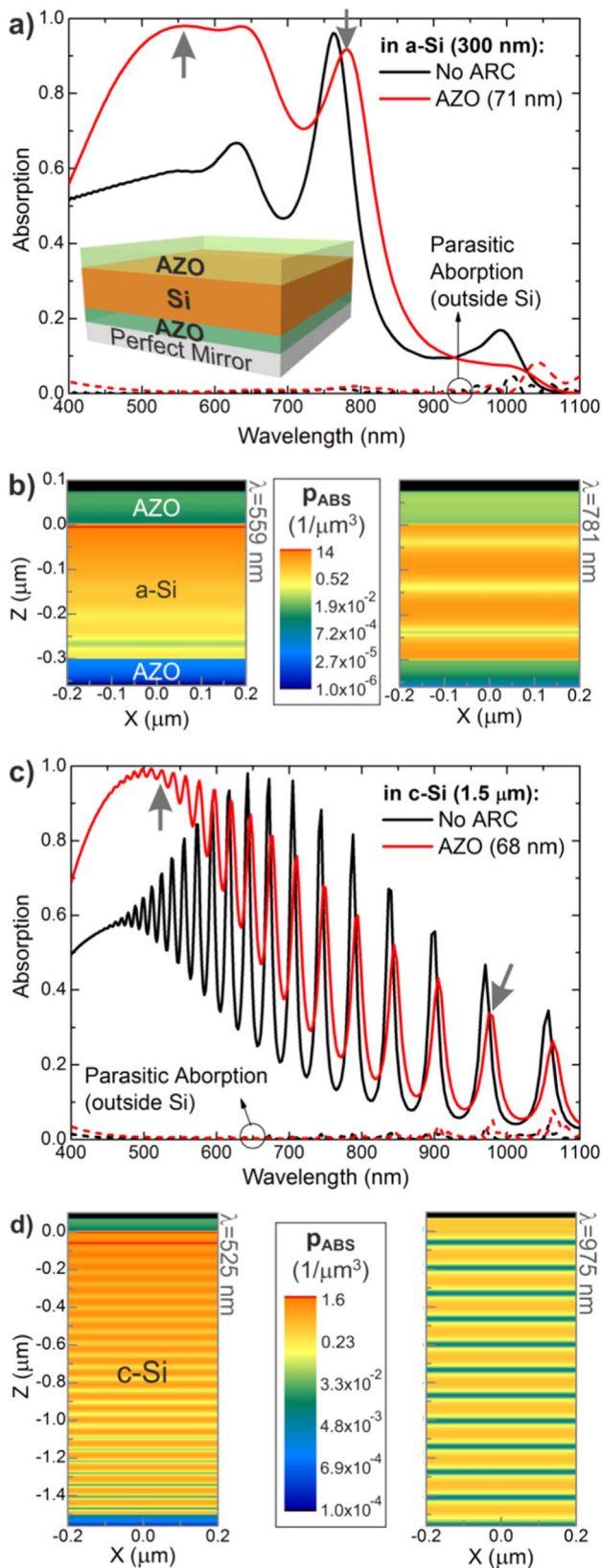
Fig. 2. a) Spectra of the light absorption occurring in the 300 nm a-Si layer (*solid lines*) and in the AZO layers (*dashed lines*) of the structure depicted in the inset. The spectrum attained with the optimized ARC (*in red*) is compared with that of no ARC (*black*). b) Log scale distribution of the absorption per unit volume (p_{ABS}) along the *xz* cross-sectional plane of the structure, at the wavelengths (λ) of the absorption peaks marked by the grey arrows in a). The origin of the *z* axis is at the Si top surface. Figures c,d) are identical to a,b) but for the case of a 1.5 μm thick c-Si absorber layer.

effective strategy to broaden and enhance (both spectrally and angularly) the LT effects [1]. Such structures serve as an effective medium on the surface whose refractive index can be gradually varied to minimize reflection, while their geometry can resonantly interact with the impinging light to produce strong scattered fields that are preferentially directed into the higher-index absorber layer with high mode density. Therefore, the photonic structures should be integrated in the cells' front TCO, to form a composed nanostructured ARC that simultaneously provides broadband anti-reflection and scattering functionalities [27].

This section presents the optimizations for a square array, with the unit cell structure depicted in Fig. 1, composed of spheroidal particles partially embedded in the front AZO layer with thickness *t*. We start by investigating the following parameters of the spheroids: real refractive index N_R (wavelength-independent) and semi-axes R and R_Z. Initially, a certain separation was considered between the bottom point of the particle and the Si top surface, by a distance $d > 0$. However, the optimizations performed on such structure always converged to a design with $d=0$, meaning that the absorption in the Si layer is maximized when the spheroid is in contact with the Si surface and has the AZO material on the sides. As such, the value of d is not presented among the best parameters of these structures, indicated in row B1 of Table 1, since it is the same ($d=0$) for all cases.

The optimization algorithm converged to structures that produce J_{SC} enhancements of 20% and 41%, relative to the optimal ARC cases of row A2, respectively in 300 nm a-Si and 1.5 μm c-Si. The optimal $N_R=2.48$ is close to that of TiO$_2$ which is, in fact, regarded as one of the preferential materials for front LT structures [27,28]. This is due to the TiO$_2$ low optical absorption coupled to a high real refractive index, relative to other dielectric materials. Therefore, this is the material that will be henceforth considered for the particles. Row B2 of Table 1 presents the results of the optimizations repeated with particles made of TiO$_2$, yielding almost as high J_{SC} values as those with the optimum lossless $N_R=2.48$ material.

Fig. 3a and c shows the light absorption of the two optimized structures with $N_R=2.48$ and TiO$_2$ spheroids, respectively on the a-Si and c-Si cells. In all cases the particles considerably broaden the absorption in the Si layers, particularly in the near-bandgap NIR spectral range, relative to the structures of Fig. 2 with an optimized ARC. The absorption curves attained with both particle materials are similar, but the non-zero imaginary component of the TiO$_2$ refractive index causes a higher parasitic absorption in such material mainly for wavelengths < 550 nm. That is why the resulting J_{SC} in row B2 of Table 1 are slightly lower than those of row B1. The parasitic absorption is practically negligible in the 550–750 nm range, but increases for longer wavelengths. These long wavelength losses take place mainly in the AZO layers [5], not inside the particles, due to the characteristic free carrier absorption of TCO materials in the NIR, as visualized in the p_{ABS} distributions on the right of Fig. 3b and d. A significant absorption in the AZO layers is also shown in the distributions on the right of Fig. 2b, and d. However, the LT effects of the particles in Fig. 3 can boost such NIR absorption, not only due to the highly intense near-fields occurring in the particles' vicinity but also due to their coupling with the rear mirror which has a stronger effect in the bottom AZO layer.

The presence of both top and bottom AZO layers is required for electrical purposes, for passivation and contact; but the top AZO also plays an important optical role since it assists in the coupling of the near-field light between the spheroid and the Si film. Without the top AZO ($t=0$) there would exist an empty region between the bottom curved surface of the spheroid and the Si, which would increase the reflected light and the parasitic absorption inside the particle. In fact, the optimization algorithm converges to values of t that maximize such near-field coupling
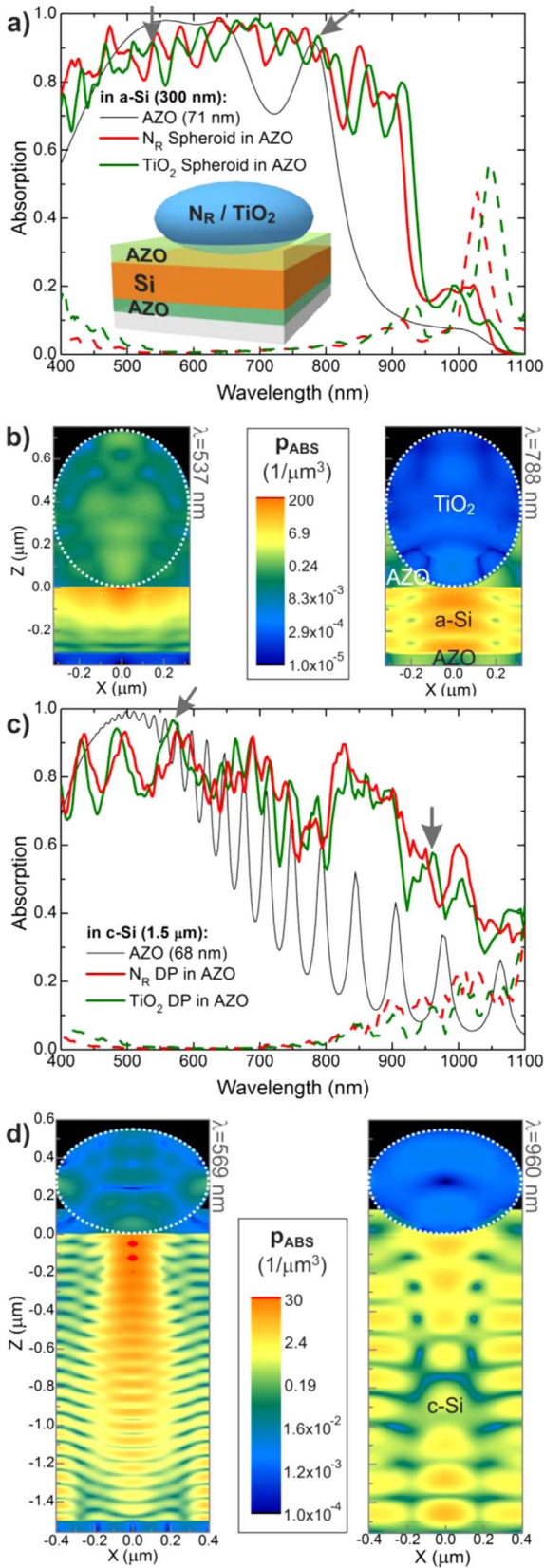
Fig. 3. a) Absorption in the 300 nm a-Si layer (*solid lines*) and in the other materials (*dashed lines*) of the structure depicted in the inset. We consider spheroids with the optimal refractive index $N_R = 2.48$ and made of TiO$_2$. The spectra are compared with that (*black line*) of the optimized AZO ARC in Fig. 2. b) Log scale distributions of p$_{ABS}$ along the *xz* plane (at y=0) of the structure with the TiO$_2$ particle, at the wavelengths of the absorption peaks marked by the grey arrows in a). The dotted ellipses indicate the perimeter of the TiO$_2$ spheroid. Figures c,d) are identical to a,b) but considering a 1.5 μm thick c-Si layer.

(rows B of Table 1), by keeping the AZO top surface below but not far from the equator of the spheroids. That is why the optimal t values are higher for the higher R_Z particles, but always below R_Z.

Regarding the particle geometries, a prolate ($R_Z > R$) shape is preferential for the 300 nm a-Si cells while an oblate shape ($R_Z < R$) is advantageous for the thicker 1.5 μm c-Si cells. Wavelength-sized dielectric objects can act as near-field lenses concentrating the forward scattered light in a jet-like region located along the incidence axis [36]. The laws of such focusing are quite distinct from those of macroscopic lenses, since it is formed by the regions of constructive interference occurring in the transmitted electromagnetic waves below the particle [29]. The higher is N_R the more localized can be the focal region, and the higher is its field magnitude. However, this shifts the focus closer to the particle center. The position and extension of the focus can be also controlled by the particle shape. A higher *oblateness* (flatness) takes the near-field focal region further away from the bottom surface of the particle and broadens its spatial coverage. Therefore, oblate spheroids are advantageous to increase absorption in a cell with a thick absorbing layer, such as the case of Fig. 3c and d. With a thinner Si layer it is better to have a more localized and intense focal region beneath the particle, which justifies the convergence to a prolate in the case of Fig. 3a and b. Such effects are clearly visualized in the p$_{ABS}$ distributions on the left of Fig. 3b and d. The prolate on the 300 nm a-Si film of b) produces a highly intense hot spot in the Si top surface which reaches a maximum p$_{ABS} = 249.4$ μm^{-3}, whereas the oblate on the 1.5 μm c-Si film of d) generates a much broader plume-like focal region with a lower maximum (p$_{ABS} = 33.6$ μm^{-3}) but extending throughout the entire depth of the film.

As discussed later in Section 4, such plume-like near-field focal region occurs mainly for wavelengths in the visible range (left of Fig. 3b and d). In the NIR, due to the lower particle sizes relative to λ, far-field scattering effects become more prominent. The low absorption coefficient of Si in this spectral range allows the scattered light to travel a long distance along the Si layer, thereby interfering with the scattered waves coming from other particles. Therefore, the *Fabry Perot* interference patterns in the right plots of Fig. 3b and d are more complex that those of Fig. 2b and d, since they result from interference occurring both in the in-plane and normal directions which creates the observed regularly distributed hot spots characteristic of the long-wavelength range.

3.3. TiO$_2$ semi-spheroids

A major drawback of the LT design of the previous Section 3.2 is the refractive index mismatch existing in the AZO-filled region between the spheroid and the Si layer, which worsens the light in-coupling towards the Si and increases the reflection. Therefore, even though the use of spheroidal particles can be advantageous to simplify the fabrication processes (as referred in the beginning of this section), this geometry is not the ideal since the curvature of the spheroids' bottom surface keeps an undesired separation between the particle and the absorber material. A better light coupling can be obtained with truncated spheroids having the truncation plane on the top Si surface.

The optimization algorithm was repeated with spheroids truncated at an arbitrary height (semi-spheroids). For that, the algorithm allowed the particles to "sink" a variable distance $d < 0$ in the Si layer, but eliminating the overlapping volume of the particle below the Si surface. TiO$_2$ is the particle material considered henceforth, in order to take a realistic absorbing dielectric medium with a refractive index close to the optimal one obtained in the previous sub-section. All optimizations led to designs with $d \approx -R_Z$, meaning that the preferential particle geometry is a half-spheroid with the equator on the plane of the Si surface, as
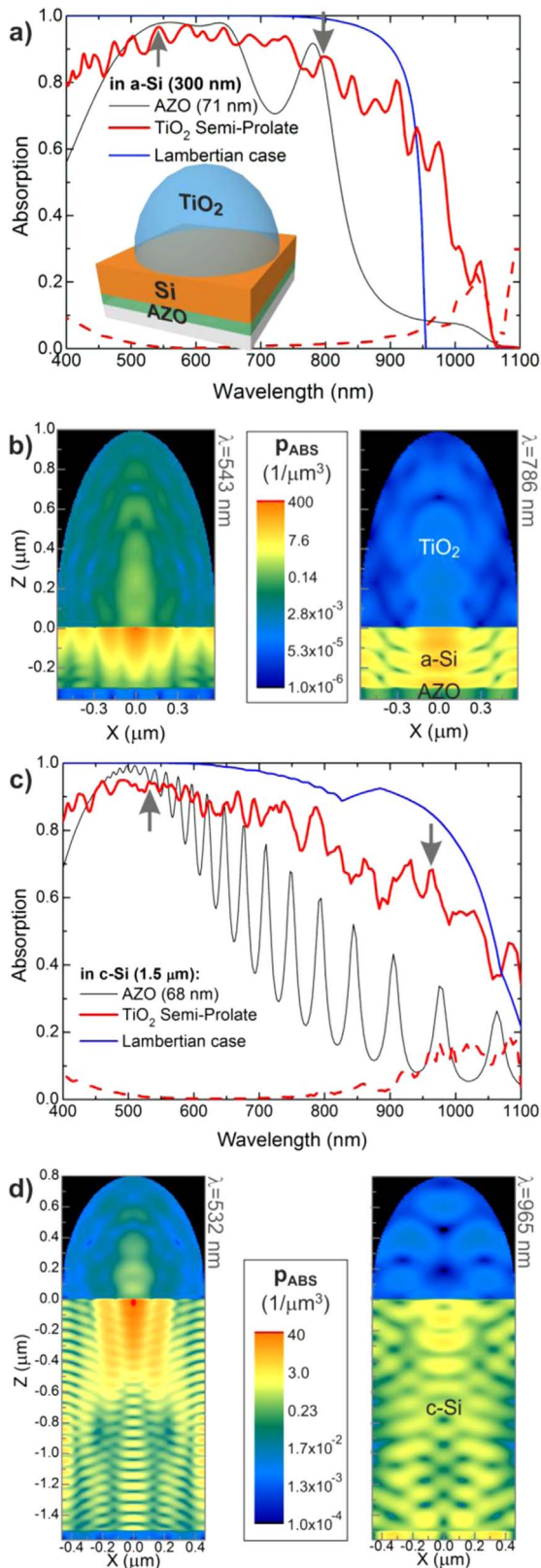
Fig. 4. a) Absorption in the 300 nm a-Si layer (*solid lines*) and in the other materials (*dashed lines*) of the structure depicted in the inset. We consider the case of TiO$_2$ half-spheroids with the base on the top surface of the Si layer. The spectrum (*red line*) is compared with that (*black line*) of the optimized AZO ARC in Fig. 2 and with the absorption, calculated in the geometrical optics regime, produced with an ideal *Lambertian* surface instead of the particles (*blue line*). b) Log scale distribution of p$_{ABS}$ along the *xz* plane (at y=0) of the structure, at the wavelengths of the peaks marked by the arrows in a). Figures c,d) are identical to a,b) but considering a 1.5 μm thick c-Si layer.

sketched in the inset of Fig. 4a. The simulations also converged to designs without front AZO layer (t=0). This is expected because in this case there is no empty region between the bottom of the particle and the Si layer (as in Section 3.2) that could beneficiate from a dielectric medium with refractive index higher than air. So, with the present geometry, the top AZO can no longer assist in the light coupling since this is better achieved by the TiO$_2$ shape alone.

As such, the LT structures analyzed henceforth are TiO$_2$ half-spheroids with height R_Z and base radius R. Since they are determined by only two parameters, the optimum was obtained by performing 2D sweeps of these variables within their allowed domain. The sweep contour plots, presented in Section S3 of the Supplementary Material, yield maxima for the parameters in row C of Table 1. The corresponding absorption spectra and spatial profiles of the optimal structures are shown in Fig. 4.

The p$_{ABS}$ profiles in Fig. 4b and d resemble those of Fig. 3b and d but have higher values along the Si depth. The p$_{ABS}$ maxima at the top of the Si layer, in the left of Fig. 4b and d, are 431.1 and 42.8 μm^{-3}, respectively; considerably above those reported previously. Therefore, the absorption curves of Fig. 4a and c attained with the half-spheroids are closer to 1 than with the previous designs. These curves are compared with those obtained in the geometrical optics regime considering an ideal *Lambertian* front surface as the LT mechanism. Even though the geometrical regime is not applicable to the present structures involving wavelength-sized features, it is usual to take it as a LT reference to understand the physical differences arising from the wave optics regime. A clear difference observed in Fig. 4a and c is that the absorption enhancement produced by wavelength-sized particles extends to longer wavelengths in the NIR, mainly due to the scattered light trapped within the thin Si layers. However, the Si absorption in most part of the spectrum and the J$_{SC}$ values achieved with the optimized TiO$_2$ half-spheroids remain below the *Lambertian* limits (row E of Table 1). This suggests that there is still room for further investigation of advanced LT designs able to reach or even surpass the conventional limits [1].
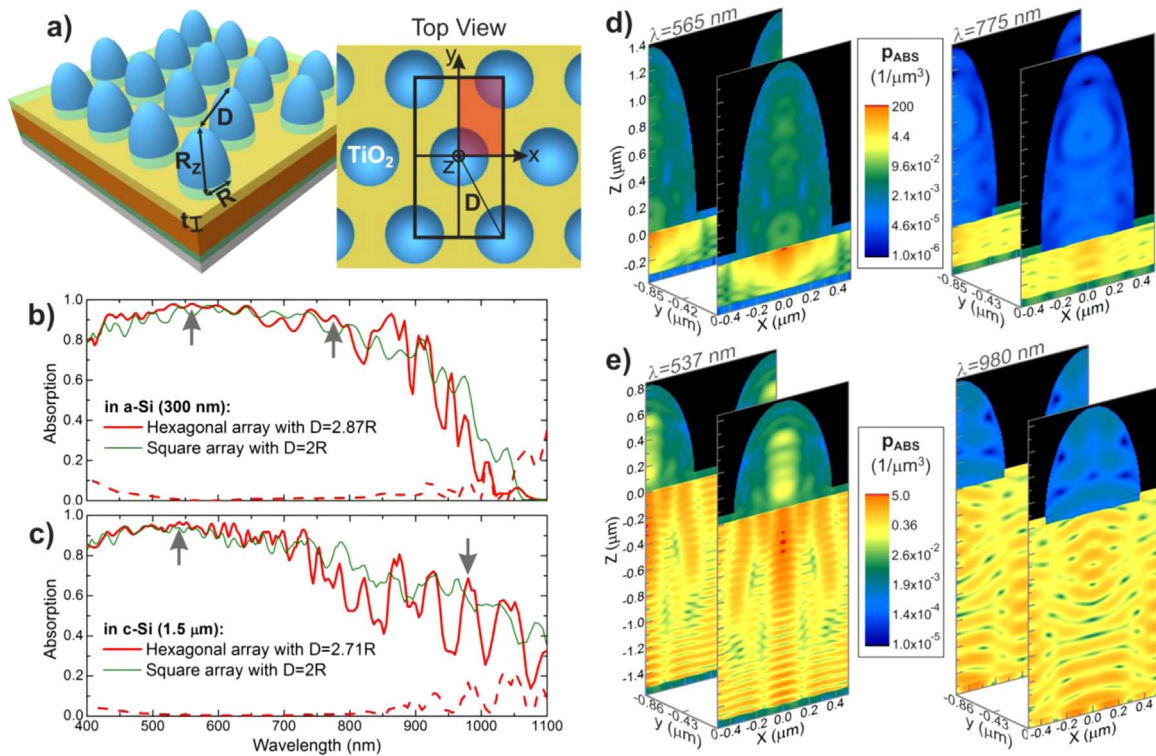
3.4. Hexagonal array of TiO$_2$ half-spheroids

The unit structures considered in the previous sub-sections correspond to the period of square arrays of adjacent particles, as described in Section 2 (see Fig. 1), with inter-particle distance D=2R. We are now interested in analyzing an hexagonal array of TiO$_2$ half-spheroids incorporated in the AZO ARC layer, as sketched in Fig. 5a, with the inter-particle distance D as an additional optimization parameter.

The hexagonal array was chosen in order to consider a structure that can be potentially fabricated by large-scale and inexpensive processes such as colloidal lithography [20,28]. This technique uses long-range ordered monolayer arrays of spheres as a mask for further pattern transfer. Such spheres are self-assembled in hexagonal arrays whose inter-particle distance can be tuned by dry-etching post-processes, so the final patterns maintain such periodicity [1,17,22,28].

The periodicity of the hexagonal lattice allows reducing the simulation to the rectangular unit cell represented in the top view of Fig. 5a. The symmetry of the unit cell allows the computational region to be further reduced to the volume in the first quadrant marked in red, by applying appropriate symmetric and anti-symmetric boundary conditions in the *y* and *x* boundaries (see Section 2).

The results of the optimization algorithm applied to this structure are shown in row D of Table 1, which are now compared with the simulations of the previous sub-Section 3.3 (row C). The optimization converged to distances D above the particles diameter (> 2R), thereby avoiding the overlap between the regions of

Fig. 5. a) Sketch of the hexagonal array of TiO$_2$ half-prolates showing the parameters considered for optimization, being R the semi-minor axis on the plane of the Si top surface, R_Z the semi-major axis (height), t the top AZO thickness and D the inter-particle distance. The rectangle represented in the top view, centered at the origin, is the unit cell (period) of the structure whose symmetry allows the computed region to be reduced to the volume in red. b,c) Absorption in the Si layer (*solid red line*) and the parasitic losses (*dashed red line*), respectively for a 300 nm a-Si and a 1.5 μm c-Si absorber. The curves are compared to those of the previous case of Fig. 4 (*green line*). d,e) Log scale distributions of p$_{ABS}$ for the wavelengths of the peaks marked by the arrows in b,c), respectively. For each wavelength the p$_{ABS}$ xz profile is shown for two planes of the array, located at y=0 and at the y boundary of the unit cell.

stronger near-fields around the spheroids that can cause dissipative inter-particle effects. Such parasitic effects can become more pronounced in an hexagonal array, relative to a square array, due to its higher packing density. Due to the inter-particle spacing, the optimal top AZO thicknesses t are no longer zero (as in the previous case) and take values close, but slightly below, those of the optimal ARCs (row A2). This ensures that there is an effective anti-reflection in the flat regions between the particles. The particle geometries converged to more elongated prolate shapes, with smaller R and bigger R_Z. A lower R reduces the parasitic inter-particle near-field effects and a higher elongation provides a smoother variation of the effective index gradient towards the Si layer, thereby improving the anti-reflection. This is evidenced in the absorption curves of Fig. 5b and c, showing that the present hexagonal array outperforms the array of Fig. 4 at shorter wavelengths (< 600–700 nm, where anti-reflection effects are dominant), but performs worse in the longer wavelengths (> 700 nm). The better performance of the array of Section 3.3 at long wavelengths, causing the slightly higher J$_{SC}$ values (see Table 1), is attributed to its stronger forward scattering effects, as explained in the next section.

4. Discussion of results

The absorption enhancement produced by the front LT elements on the Si absorber layers is caused by two optical mechanisms: anti-reflection and scattering. These mechanisms operate simultaneously and their effects on the electric field distribution within the absorber change across the spectral range of interest, as sketched in the diagram of Fig. 6. Two main spectral regions can be identified for each mechanism, at short and long
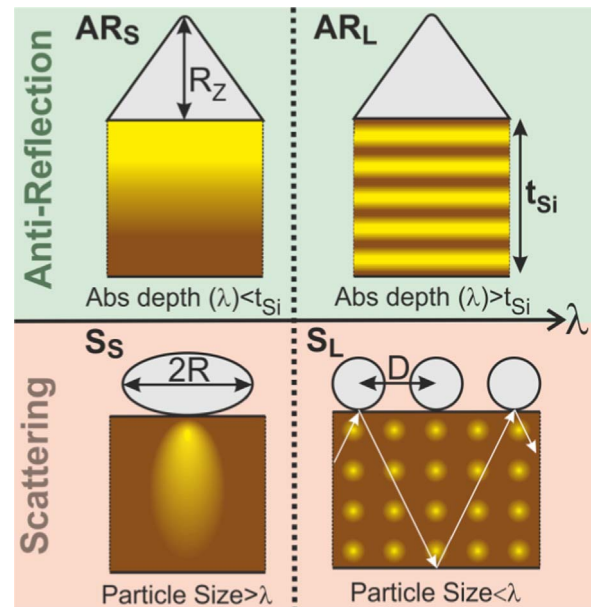
Fig. 6. Illustrative diagram of the characteristic E-field enhancement profiles resulting from the LT mechanisms generated by the dielectric front structures of Section 3. The profiles produced by anti-reflection and scattering effects exhibit a smooth transition (represented by the dashed line) within the considered wavelength range. The transition regarding anti-reflection roughly occurs when the absorption depth in the Si layer surpasses the layer thickness (at λ∼720 nm for 300 nm a-Si and λ∼570 nm for 1.5 μm c-Si); whereas with scattering the transition is mainly determined by the characteristic particle size (∼2R) relative to λ. The main parameter influencing the absorption enhancement in each of the four profiles is indicated by the black arrows.

wavelengths, thus leading to the four types of field enhancement profiles (AR_S, AR_L, S_S and S_L) depicted in Fig. 6. It is important to point out that such transitions are not abrupt, so the p_{ABS} profiles observed in the previous section actually contain a mixture of different contributions from each of the four types of profiles. However, since the effects are intimately related, it is difficult to quantify the weights of these contributions separately [13,35]. In the following sub-sections each LT mechanism is described in more detail.

4.1. Anti-reflection action

The suppression of outgoing waves and the in-coupling of light towards the absorber occurs due to a better wave-impedance matching at the cell front. For this mechanism, the preferential LT structures are cone/pyramid-like elements (sketched on the top of Fig. 6), with a real-valued refractive index as close as possible to that of the absorber material and the highest possible height (R_Z), in order to have the most gradual variation of effective index from air towards the absorber layer. This increases absorption mainly in the short wavelength portion of the spectrum (AR_S in Fig. 6), leading to the peaks at the left-side arrows in the plots of Fig. 2a and c.

When the absorption depth is higher than the absorber thickness (AR_L), the light waves reflected between the top and bottom Si surfaces establish a *Fabry Perot* interference pattern, along the incidence direction, which enhances the absorption in the in-plane regions of constructive interference [1]. The *Fabry Perot* resonances of the thin film Si cavity result in the peak at 781 nm in 300 nm a-Si (Fig. 2a) and in the abrupt peaks observed in 1.5 μm c-Si (Fig. 2c). Such peaks are originated by the absorber thin film alone, so their spectral position and shape are chiefly determined by the Si thickness (t_{Si}) and not so much by the ARC or back reflector.

Among the LT structures investigated in this work, the TiO_2 half-prolates of Sections 3.3 and 3.4 are those with the best broadband anti-reflective properties, as evidenced by their high absorption around 0.9 for $\lambda < 800$ nm. The spheroids of Section 3.2 exhibit inferior anti-reflection action (lower absorption at short wavelengths), due to their bottom curvature that does not allow a monotonously increasing index gradient towards the Si, which is the main reason for their lower J_{SC} relative to the designs of Sections 3.3 and 3.4.

4.2. Scattering action

The high-index particles with sizes on the order of the wavelengths exhibit pronounced scattering cross sections [31] and, consequently, strong forward scattered fields that can enhance the absorption in the Si layer in distinct ways for wavelengths below or above the particles' size. For the shorter wavelengths (S_S in Fig. 6), the particles produce a lens effect in their forward scattered near-field forming an intense plume-like focal region along the illumination direction [29,36]. The wider the particle diameter ($2R$) the higher can be its scattering cross section and, consequently, the stronger is the light focusing effect on the Si film. However, as discussed in Section 3.2, the particles' aspect ratio determines the extension and strength of such focus. So, flat (oblate) shapes are preferable for the 1.5 μm c-Si absorber layers, but more elongated (prolate) shapes are preferable for the thinner 300 nm a-Si layers, since the extension of the focal region should match the depth of the Si layer.

For the longer wavelengths (S_L), it is the scattered far-fields that can produce the most significant absorption enhancement, as the light waves are scattered with an angular distribution that directly results in a path length enhancement for the light inside the cell. In addition, at these wavelengths the absorption depth in the Si

layer becomes comparable or higher than the inter-particle spacing, so the collective scattering of the periodic particle array functions as a 2D grating providing the in-plane momentum needed for the light to couple to confined waveguided modes traveling within the Si slab [5,21,31]. This effect mainly depends on the array pitch (D) and leads to particularly intense absorption enhancement in a discrete set of wavelengths where the mode matching occurs, resulting in the sharp peaks in the NIR region of the absorption spectra of the cells with particles. The interference between the waves traveling along the layer plane, and bouncing with the top and bottom surface of the cell, establishes a *Fabry Perot* pattern composed of hot spots distributed along the layer at the locations of constructive interference [1,27], as depicted in Fig. 6. Such signature of the S_L profile can be clearly observed in the p_{ABS} distributions in 1.5 μm c-Si on the right of Figs. 3d and 5d, in which $2R < \lambda$ and the absorption depth in Si (> 10 μm) is much higher than D. This is also evidenced by the abrupt peaks of the corresponding absorption curves of Figs. 3c and 5c for $\lambda > 800$ nm. In the p_{ABS} distribution of Fig. 4d at $\lambda = 965$ nm, the absorption depth in Si is also much higher than D ($= 2R$ in this array), but the particle size is close to the wavelength ($2R \sim \lambda$). Therefore, in this case of Section 3.3 there is still a significant contribution from the light focusing effect (S_S) in the absorption enhancement even at the longer wavelengths. That is why the absorption curves of this structure are relatively smoother in the NIR range, as seen in the plots compared in Fig. 5c, which results in its higher J_{SC} enhancement (see Table 1).

Apart from the aforementioned differences, all the optimized particle structures of Section 3 provide comparably strong scattering, as shown by the extension of the NIR absorption to long wavelengths, which allowed enhancements superior to the *Lambertian* scattering surface within a narrow near-bandgap spectral range (see Fig. 4a and c), and by the disappearance of the dips in absorption (e.g. at 723 nm for the a-Si film) present in the structures without particles (black curves in Figs. 3 and 4). Such dips originated from light interference established within the Si layer in the incidence direction (AR_L effect), and are quenched in the structures with particles due to the scattering of light to more horizontal angles.

Both anti-reflection and scattering mechanisms beneficiate from a high real part of the refractive index (N_R) of the photonic elements and a low imaginary part. A high N_R favors the anti-reflection of cone/dome-like structures because it allows a better matching with the high-index absorber layer (Si, with $N_R \sim 4$). It also leads to increased interaction cross sections of the particles and thereby allows stronger far and near field scattering. Therefore, the optimizations pointed to high-index lossless materials such as TiO_2.

Concerning the particles geometry, the more vertically-elongated structures favor anti-reflection, while flat ones can exhibit stronger scattering cross sections and thereby favor effects S_S and S_L of Fig. 6 [1]. Tuning the shape and size of the photonic elements allows their LT contribution to be stronger in different portions of the spectrum, which is important to adapt them to different types of solar cells. For instance, cells with thin a-Si layers exhibit less NIR response relative to c-Si, so they beneficiate from higher particle elongations that strengthen their anti-reflection action at the UV–vis range. Devices with a broader response in the NIR, as thick c-Si or quantum dot solar cells [12,16,37], would benefit more from scattering mechanisms tuned to the long wavelengths.

5. Conclusions

Most light trapping (LT) schemes integrated so far in solar cells imply increasing the absorber layer roughness and the density of
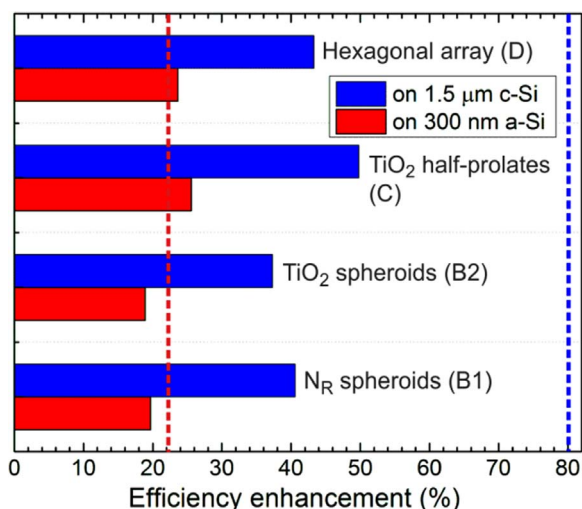
Fig. 7. Estimated efficiency enhancements, relative to the optimized single-layer ARC case (Fig. 2, row A2 of Table 1), attained with the distinct light trapping structures analyzed in Section 3. The labels in brackets indicate the corresponding row in Table 1. The vertical dashed lines represent the values of enhancement attained for the *Lambertian* case in the regime of geometrical optics, considering the 300 nm a-Si (*red line*) and 1.5 μm c-Si (*blue*) absorber layers. Such *Lambertian* enhancement values are indicated in Fig. S1 of the Supplementary Material and are determined relative to the corresponding structures without light trapping.

bulk and surface defects, since they are mainly based in nanostructuring the absorber and/or the substrate via etching processes which create surface textures or photonic patterns composed by distinct types of corrugations [5,10,15,21,22,25,31]. Such schemes strongly rely on surface doping and passivation solutions to prevent performance degradation due to carrier recombination, which usually limits the designs from reaching their full optical potential. Therefore, here a promising strategy was investigated that consists in optimizing photonic elements on top of unstructured planar absorber layers, implemented in the cells' front. This way, the voltage supplied by the devices is expected to be maintained (possibly even increased) while substantially enhancing the output current. Hence, the efficiency gains resulting from the incorporation of the LT structures are expected to be similar to the J_{SC} enhancements attained here. Such enhancement values were calculated relative to the optimized ARC layers of Section 3.1 and are indicated by the bars in Fig. 7.

The higher enhancements are predicted for the 1.5 μm c-Si cells, reaching almost 50% for the TiO$_2$ half-prolates design of Section 3.3. The enhancements are lower for the a-Si cells because it is a direct bandgap semiconductor whose absorption coefficient rises rapidly above the bandgap, which limits the spectral range where the long-wavelength LT effects can provide substantial improvements. Nevertheless, both half-prolate structures (Sections 3.3 and 3.4), operating on the thin a-Si cells in the wave optics regime, allow enhancements superior to those (dashed lines in Fig. 7) predicted by the theoretical limit of *Lambertian* surfaces in the regime of geometrical optics (see Section S1 of the Supplementary Material), and also higher than previous dielectric wavelength-sized structures patterned on top of a-Si:H cells such as close-packed sphere arrays (~10% enhancement [17]).

Although we focused here in a-Si and c-Si absorber materials, the insights gained in this study on the effects of dielectric photonic structures are generic and can be applied to virtually any type of thin film solar cell, by careful adaptation of the geometrical parameters.

Acknowledgments

Appendix A. Supporting information

Supplementary data associated with this article can be found in the online version at http://dx.doi.org/10.1016/j.nanoen.2016.05.038.

References

[1] M.L. Brongersma, Y. Cui, S. Fan, Light management for photovoltaics using high-index nanostructures, Nat. Mater. 13 (5) (2014) 451–460.
[2] A. Shah, Thin-Film Silicon Solar Cells, EFPL Press, Lausanne, Switzerland, 2010.
[3] H. Águas, et al., Thin film silicon photovoltaic cells on paper for flexible indoor applications, Adv. Funct. Mater. 25 (23) (2015) 3592–3598.
[4] A. Vicente, et al., Solar cells for self-sustainable intelligent packaging, J. Mater. Chem. A 3 (25) (2015) 13226–13236.
[5] V.E. Ferry, et al., Optimized spatial correlations for broadband light trapping nanopatterns in high efficiency ultrathin film a-Si:H solar cells, Nano Lett. 11 (10) (2011) 4239–4245.
[6] M. Despeisse, et al., Optimization of thin film silicon solar cells on highly textured substrates, Physica Status Solidi A 208 (8) (2011) 1863–1868.
[7] P. Kowalczewski, et al., Light trapping and electrical transport in thin-film solar cells with randomly rough textures, J. Appl. Phys. 115 (19) (2014).
[8] A. Ingenito, O. Isabella, M. Zeman, Experimental demonstration of 4n2 classical absorption limit in nanotextured ultrathin solar cells with dielectric omnidirectional back reflector, ACS Photonics 1 (3) (2014) 270–278.
[9] K.M. Park, M.B. Lee, S.Y. Choi, Investigation of surface features for 17.2% efficiency multi-crystalline silicon solar cells, Sol. Energy Mater. Sol. Cells 132 (2015) 356–362.
[10] M.J. Mendes, et al., Broadband light trapping in thin film solar cells with self-organized plasmonic nano-colloids, Nanotechnology 26 (13) (2015) 135202.
[11] M.J. Mendes, et al., Colloidal plasmonic back reflectors for light trapping in solar cells, Nanoscale 6 (9) (2014) 4796–4805.
[12] A. Mellor, et al., Upper limits to absorption enhancement in thick solar cells using diffraction gratings, Progress Photovolt. Res. Appl. 19 (6) (2011) 676–687.
[13] C.S. Schuster, et al., Plasmonic and diffractive nanostructures for light trapping?an experimental comparison, Optica 2 (3) (2015) 194–200.
[14] A. Bozzola, M. Liscidini, L.C. Andreani, Photonic light-trapping versus Lambertian limits in thin film silicon solar cells with 1D and 2D periodic patterns, Opt. Express 20 (S2) (2012) A224–A244.
[15] F. Priolo, et al., Silicon nanostructures for photonics and photovoltaics, Nat. Nano 9 (1) (2014) 19–32.
[16] A. Mihi, et al., Coupling resonant modes of embedded dielectric microspheres in solution-processed solar cells, Adv. Opt. Mater. 1 (2) (2013) 139–143.
[17] J. Grandidier, et al., Solar cell efficiency enhancement via light trapping in printable resonant dielectric nanosphere arrays, Physica Status Solidi A 210 (2) (2013) 255–260.
[18] S. Morawiec, et al., Broadband photocurrent enhancement in a-Si:H solar cells with plasmonic back reflectors, Opt. Express 22 (S4) (2014) A1059–A1070.
[19] S. Morawiec, et al., Self-assembled silver nanoparticles for plasmon-enhanced solar cell back reflectors: correlation between structural and optical properties, Nanotechnology 24 (26) (2013) 265601.
[20] D. Zhou, et al., Optimization of the optical properties of nanostructured silicon surfaces for solar cell applications, J. Appl. Phys. 115 (13) (2014) 134304.
[21] P. Spinelli, A. Polman, Light trapping in thin crystalline Si solar cells using surface Mie scatterers, IEEE J. Photovolt. 4 (2) (2014) 554–559.
[22] H. Sai, et al., Triple-junction thin-film silicon solar cell fabricated on periodically textured substrate with a stabilized efficiency of 13.6%, Appl. Phys. Lett. 106 (21) (2015) 213902.
[23] E.R. Martins, et al., Deterministic quasi-random nanostructures for photon control, Nat. Commun. 4 (2013) 2665.
[24] A. Bozzola, P. Kowalczewski, L.C. Andreani, Towards high efficiency thin-film crystalline silicon solar cells: the roles of light trapping and non-radiative recombinations, J. Appl. Phys. 115 (9) (2014) 094501.
[25] C. Trompoukis, et al., Photonic nanostructures for advanced light trapping in thin crystalline silicon solar cells, physica Status Solidi A 212 (1) (2015) 140–155.

[26] M.J. Mendes, et al., Near-field scattering by dielectric spheroidal particles with sizes on the order of the illuminating wavelength, J. Opt. Soc. Am. B 27 (6) (2010) 1221–1231.

[27] X.H. Li, et al., Light trapping in thin-film solar cells via scattering by nanostructured antireflection coatings, J. Appl. Phys. 114 (4) (2013) 044310.

[28] M. Karg, et al., Colloidal self-assembly concepts for light management in photovoltaics, Mater. Today 18 (4) (2015) 185–205.

[29] M.J. Mendes, et al., Light concentration in the near-field of dielectric spheroidal particles with mesoscopic sizes, Opt. Express 19 (17) (2011) 16207–16222.

[30] Lumerical Solutions, Inc. ⟨http://www.lumerical.com/tcad-products/fdtd/⟩.

[31] C. van Lare, et al., Dielectric scattering patterns for efficient light trapping in thin-film solar cells, Nano Lett. 15 (8) (2015) 4846–4852.

[32] Refractive Index Database, retrieved Feb. 2015. Available from: ⟨http://refractiveindex.info⟩.

[33] E. Palik, Handbook of Optical Constants of Solids, Academic Press, San Diego, CA, 1997.

[34] J. Pond, M. Kawano, Virtual prototyping and Optimization of Novel Solar Cell Designs, 2010.

[35] D.M. Callahan, J.N. Munday, H.A. Atwater, Solar cell light trapping beyond the ray optic limit, Nano Lett. 12 (1) (2011) 214–218.

[36] N. Horiuchi, Light scattering: photonic nanojets, Nat. Photonics 6 (3) (2012) 138–139.

[37] M.J. Mendes, et al., Self-organized colloidal quantum dots and metal nanoparticles for plasmon-enhanced intermediate-band solar cells, Nanotechnology 24 (34) (2013) 345402.